Chapter 6
LEAP-ASIA-2019 Centrifuge Test at University of California, Davis

Nicholas S. Stone, Trevor J. Carey, Anthony Santana, and Bruce L. Kutter

Abstract For the LEAP-ASIA-2018 exercise, a centrifuge test was conducted in parallel at ten centrifuge facilities, including the University of California, Davis (UCD). The experiment consisted of a submerged clean sand profile oriented with a 5-degree slope subjected to 1 Hz ramped sine wave motions applied at the base of a rigid container. This paper explains several details of the experiment at UCD, including experiment results, implementation of high-speed cameras and GeoPIV software to measure slope deformation, and the presence of vertical accelerations due to the Coriolis effect and how the accelerations might affect model performance. In addition, this paper presents data and comparison for both conventional (Type A) and generalized (Type B) centrifuge scaling laws.

6.1 Introduction

The current phase of LEAP, LEAP-ASIA-2018, involved centrifuge experiments conducted at ten different research facilities, including the University of California, Davis (UCD). The experiment, similar to LEAP-UCD-2017 and LEAP-GWU-2015, consisted of a submerged clean sand deposit sloped at 5 degrees, subjected to a 1 Hz ramped sine wave ground motion inputted at the base of the rigid model container. The experiments were performed on the 1 m radius Schaevitz centrifuge at the Center for Geotechnical Modeling at UCD. The 1 m centrifuge performs shaking in

N. S. Stone · A. Santana · B. L. Kutter
Department of Civil and Environmental Engineering, University of California, Davis, CA, USA
e-mail: Trevor.Carey@civil.ubc.ca

T. J. Carey (✉)
Department of Civil Engineering, The University of British Columbia, Vancouver, Canada

the circumferential direction of the centrifuge. Detailed specifications by Kutter et al. (2019) were provided to facilitate replicability among the different centrifuge facilities. The goals of LEAP-ASIA-2018 were filling in the gaps and further extending/confirming the trends obtained in LEAP-UCD-2017 and evaluating the applicability of generalized scaling laws (Iai et al., 2005). Discussed in these proceedings are the model specifications, achieved input motions, sensor results, and unique aspects of three centrifuge models, referred to as UCD4, UCD5, and UCD6.

6.2 UC Davis Test Specific Information

6.2.1 Description of the Model and Instrumentation

The same container was used for the UCD experiments as during the LEAP-UCD-2017 exercise (Carey et al., 2020). The container dimensions are 457.2 mm (L) × 279.4 mm (W) × 177.8 mm (H). As in 2017, 25.4-mm-thick plastic plates were placed on each end wall of the rigid container to obtain the 457.2 mm length. The plastic plates were placed to ensure the soil would remain completely submerged at 1 g and the water would not spill out of the container during spinning. Figure 6.1 details the test geometry, sensor locations, PVC blocks, and approximate fluid level during spinning in model scale.

Modeling a flat surface under a radial g-field requires a curved surface with the same radius of curvature as the imposed g-field. A slope relative to the radial g-field is described theoretically by a log spiral. Carey et al. (2017) showed that a log spiral can be approximated by rotating a circular arc by 5 degrees. The maximum error in model depth between the log spiral surface and that of the circular arc is 2.2%. Figure 6.2 shows the procedure for vacuuming the curved surface using a wooden template and flat head vacuum attachment.
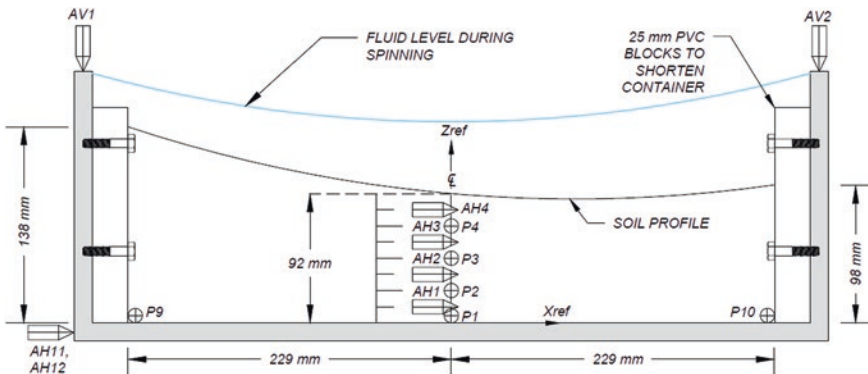

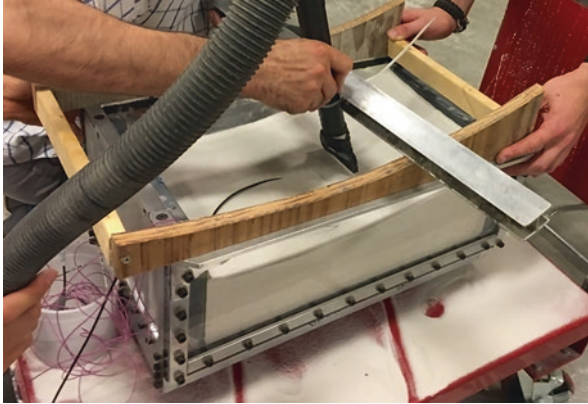**Fig. 6.1** Model geometry and sensor layout (dimensions in model scale)

Fig. 6.2 Wooden template and vacuum tool used to approximate the log spiral surface

6.2.2 Sensors

The number of sensors placed in the model was limited by the capacity of the data acquisition system; therefore, only the required pore pressure transducers (P1, P2, P3, P4, P9, and P10) and accelerometers (AH1, AH2, AH3, AH4, AH11, AH12, AV1, and AV2) were included. Specified locations of each sensor are shown in Fig. 6.1.

6.2.3 Scaling Laws

The scaling laws for LEAP-ASIA-2018 were provided by Iai et al. (2005). In these specifications, a factor μ was defined as the virtual 1 g scaling factor, leaving η as the centrifuge scaling factor, and $\mu * \eta$ as the generalized scaling factor. Figure 6.3 provides the schematic of generalized centrifuge scaling with factors μ and η. Table 6.1 provides the generalized scaling relationships for the centrifuge experiments. Two models were tested using conventional scaling laws ($\mu = 1$), while one model was tested using the generalized scaling law and a virtual scale factor of $\mu = 2$. Table 6.2 lists the scaling factors used for each experiment.

6.2.4 CPT Re-calibration

In-flight cone penetrometer (CPT) measurements were made using a device described by Carey et al. (2018b). The device uses an internal rod, protected by an outer sleeve to transmit cone tip forces to a load cell. During the final assembly of the CPT device, the internal rod was threaded into the load cell until a preload of
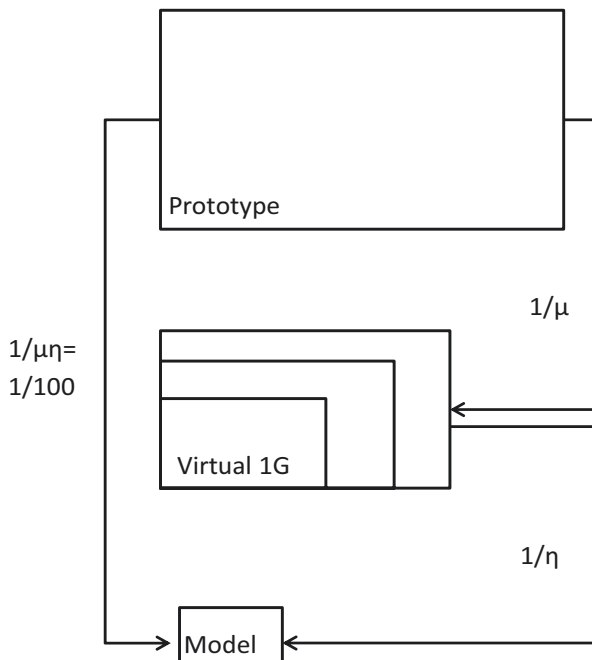
Fig. 6.3 Generalized scaling schematic

Table 6.1 Generalized scaling relationships

	(1) Scaling factors for 1 g test	(2) Scaling factors for centrifuge test	(3) Generalized scaling factors
Length	μ	η	$\mu\eta$
Density	1	1	1
Time	$\mu^{0.75}$	η	$\mu^{0.75}\eta$
Frequency	$\mu^{-0.75}$	$1/\eta$	$\mu^{-0.75}/\eta$
Acceleration	1	$1/\eta$	$1/\eta$
Velocity	$\mu^{0.75}$	1	$\mu^{0.75}$
Displacement	$\mu^{1.5}$	η	$\mu^{1.5}\eta$
Stress	μ	1	μ
Strain	$\mu^{0.5}$	1	$\mu^{0.5}$
Stiffness	$\mu^{0.5}$	1	$\mu^{0.5}$
Permeability	$\mu^{0.75}$	η	$\mu^{0.75}\eta$
Pore pressure	μ	1	μ

Table 6.2 Scaling factors used for the three UCD experiments

	Virtual 1 g scale factor, μ	Centrifuge scale factor, η
UCD4	1	43.75
UCD5	2	21.9
UCD6	1	43.75

4–9 N on the tip O-ring was achieved, using a procedure summarized by Carey et al. (2018b) and described in detail in the documents distributed with the equipment. Preloading the tip O-ring ensures the gap between the cone shoulder and sleeve is closed, and specifying the preload minimizes variable preloads. The assembled device was calibrated at the Center for Geotechnical Modeling at UCD. A calibration load cell was attached to the top of the rigid aluminum block to record the total force as the cone tip was pushed into soft plastic using a pneumatic actuator. The difference between the force measured with the CPT device load cell and calibration load cell is attributed to compression of the tip O-ring and friction between the internal bracing O-rings. Carey et al. (2018b) showed the magnitude of friction varied linearly with the cone tip force and therefore could be corrected using a calibration factor. The calibration factor was applied to the measured cone tip force, and the assembled device was checked once more to ensure the recorded force at the tip was identical to the calibration load cell. The calibration process was done prior to UCD4.

6.3   Results

6.3.1   Achieved Dry Densities

UCD performed three experiments with varying target densities. The measured dry densities were calculated by the measurement of mass and volume of the soil in the model container. A more detailed explanation of the method used to measure the volume of each model, adapted from Carey et al. (2020), is described later. Table 6.3 lists the measured dry density of each constructed model. Model construction was achieved by dry pluviation through a no. 16 sieve with three slots (Kutter et al. 2019) from a standard drop height, adjusted at each 11.4 mm lift. UCD4 and UCD5 models were pluviated through 1.2-mm-wide slots from a 660 mm drop height. UCD6 was pluviated though 10.3-mm-wide slots from a 325 mm drop height.

Table 6.3 Measured dry densities for the three UCD experiments

	Measured dry density $\left(\dfrac{\text{kg}}{\text{m}^3} \right)$
UCD4	1713
UCD5	1712
UCD6	1658

6.3.2   Achieved Sensor Locations

All sensors were placed in accordance with specifications for LEAP-ASIA-2018. Sensors were placed using the tools employed to measure locations throughout the model; therefore, initial sensor locations were within measurement error of their specified locations. Final locations of the sensors were measured during excavation following each experiment; these are listed in the LEAP-ASIA-2018 test template.

6.3.3   Achieved Ground Motions

The ground motion intensity parameter, $PGA_{effective}$, introduced by Kutter et al. (2019) was used to characterize the achieved input motions of each model. The measured input motions were filtered into their constituents: the 1 Hz signal and the superimposed higher frequencies. Then, PGA_{eff} is calculated as $PGA_{eff} = PGA_{1Hz} + \dfrac{1}{2} PGA_{HF}$. (The components of PGA_{eff} are given for the experiments in Tables 6.4a, 6.4b and 6.4c for destructive motions one, two, and three, respectively).

Table 6.4a Destructive Motion 1 PGA for the three UCD experiments

	Destructive Motion 1			
	PGA_{raw} (g)	PGA_{eff} (g)	PGA_{1Hz} (g)	PGA_{HF} (g)
UCD4	0.191	0.191	0.161	0.059
UCD5	0.154	0.150	0.131	0.038
UCD6	0.150	0.143	0.123	0.041

Table 6.4b Destructive Motion 2 PGA for the three UCD experiments

	Destructive Motion 2			
	PGA_{raw} (g)	PGA_{eff} (g)	PGA_{1Hz} (g)	PGA_{HF} (g)
UCD4	0.428	0.341	0.249	0.182
UCD5	0.341	0.299	0.241	0.117
UCD6	0.216	0.192	0.165	0.055

Table 6.4c Destructive Motion 3 PGA for the three UCD experiments

	Destructive Motion 3			
	PGA_{raw} (g)	PGA_{eff} (g)	PGA_{1Hz} (g)	PGA_{HF} (g)
UCD4	NA	NA	NA	NA
UCD5	NA	NA	NA	NA
UCD6	0.513	0.391	0.269	0.245

6.3.4 Accelerometer Readings During Destructive Motions

The acceleration time histories of the input base motions and the four central array horizontal accelerometers (AH1, AH2, AH3, and AH4) from each destructive motion are shown in Fig. 6.4. The input base motion is taken as the average of the time history recorded from AH11 and AH12. The acceleration time histories of the two vertical accelerometers (AV1 and AV2) during each destructive motion are shown in Fig. 6.5.

- UCD4

    – Destructive Motion 1: Slight amplification of the base motion occurs, especially in the top two accelerometers (AH3 and AH4). Accelerometers throughout the model remained in phase during the motion. This indicates the soil near the ground surface may have undergone some small degree of nonlinearity, but the bottom remained rigid.
    – Destructive Motion 2: Amplification of the base motion occurs in all accelerometers, with increasing amplification at shallower depths. Overall, greater amplification occurred in M2 than M1. Dilation spikes only occurred in AH4, while AH3 and AH4 both lag the base motion, indicating more severe liquefaction at shallower depths.
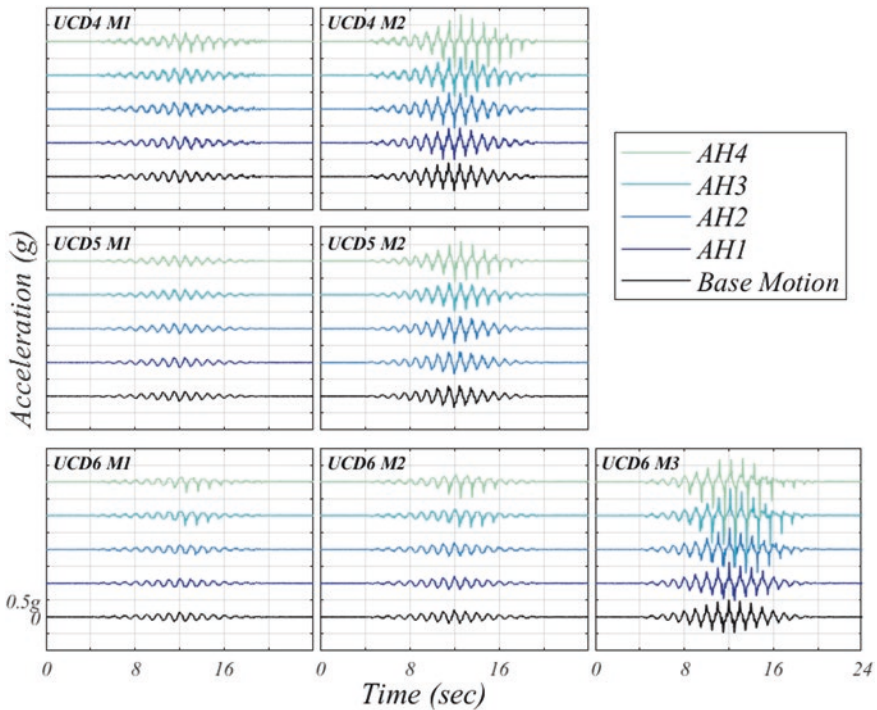
Fig. 6.4 Horizontal acceleration time histories for UCD4, UCD5, and UCD6
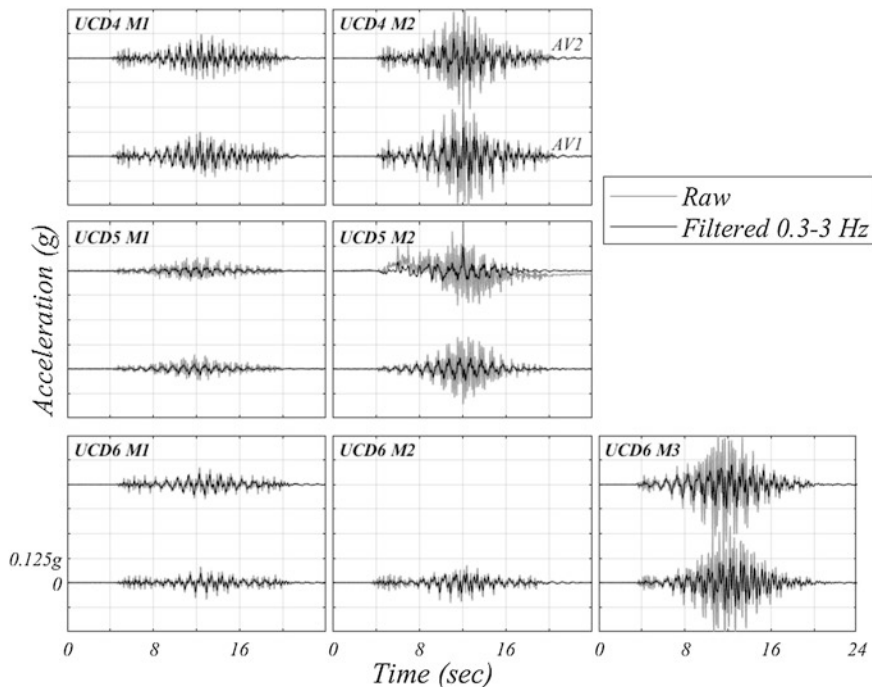
Fig. 6.5 Vertical acceleration time histories for UCD4, UCD5, and UCD6

- UCD5
  - Destructive Motion 1: No amplification or phase lag occurs at any accelerometer, indicating the model behaved as a rigid body. There is little evidence of nonlinearity or liquefaction in the acceleration time histories.
  - Destructive Motion 2: Amplification of the base motion is observed in all accelerometers, with increasing amplification at shallower depths. Similar to UCD4 M2, dilation spikes were only measured by AH4, and both AH3 and AH4 are out of phase with the base motion, indicating more severe liquefaction at shallower depths.

- UCD6
  - Destructive Motion 1: This was the smallest motion performed during the three UCD experiments. Slight amplification of the base motion occurred in AH3 and AH4 from times 12–16 s.
  - Destructive Motion 2: Amplification of the base motion occurred at AH3 and AH4. AH3 and AH4 are slightly out of phase with the base motion. This indicates liquefaction occurred at shallow depths only and at a less severe degree than other motions (e.g., UCD4 M2 and UCD5 M2). Dilation spikes during this motion are small; however, this model is less dense than UCD4 and UCD6, hence, less dilatancy is expected.

– Destructive Motion 3: Amplification of the base motion and dilation spikes occurred at each accelerometer, with increasing amplification and severity of the dilation spikes at shallower depths. AH2, AH3, and AH4 are out of phase with the base motion. This was the largest motion performed during the three UCD experiments, resulting in the most severe amplification, dilation spikes, and phase lag.

6.3.5   Excess Pore Pressures During Destructive Motions

The excess pore pressures recorded by pore pressure transducers in the central array (e.g., P1, P2, P3, and P4) are shown in Fig. 6.6, and the excess pore pressures as recorded at the container ends (P9 and P10) are shown in Fig. 6.7.
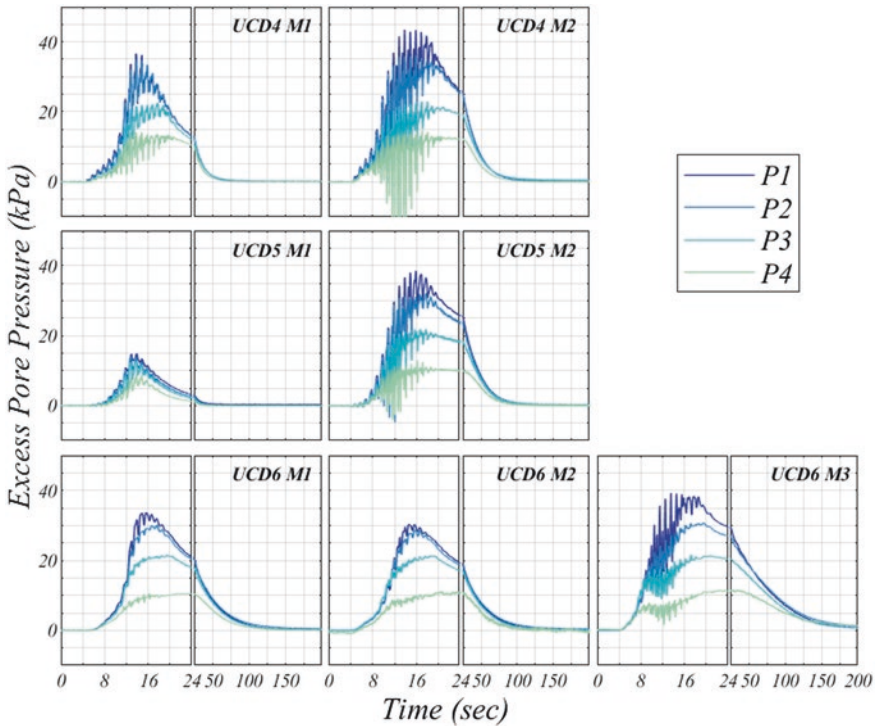
Fig. 6.6 Excess pore pressures of the central array for UCD4, UCD5, and UCD6. The initial effective stress is approximately 10, 20, 30, and 39 kPa at sensors P4, P3, P2, and P1, respectively
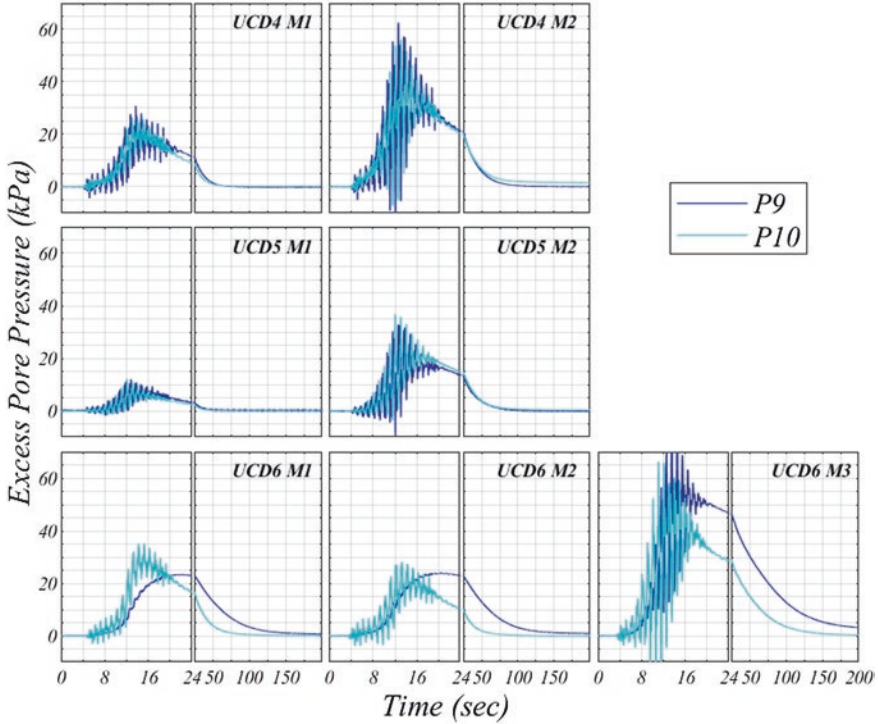
Fig. 6.7 Excess pore pressures at model ends for UCD4, UCD5, and UCD6

- UCD4
  - Destructive Motion 1: The excess pore pressure approached the initial effective stress at sensors P3 and P4, but not at P1 or P2. Zero effective stress remained after the end of the motion (at 20 s) at P4, while excess pore pressure immediately started to dissipate at P3 following the end of shaking. This implies sustained liquefaction at P4, unsustained liquefaction at P3, and no liquefaction at greater depths.
  - Destructive Motion 2: Zero effective stress was reached at sensors P2, P3, and P4. Zero effective stress sustained at P3 and P4, but not P2. This implies sustained liquefaction at P3 and P4, unsustained liquefaction at P2, and no liquefaction at the base of the container. Zero effective stress at the base of the container is difficult to reach, as no excess pore pressure is generated due to an upward hydraulic gradient.

- UCD5
  - Destructive Motion 1: Zero effective stress was not reached at any depth, indicating liquefaction did not trigger during this motion. Due to the lack of liquefaction and initially dense state, Destructive Motion 1 could likely be

considered a non-destructive event, and Destructive Motion 2 might be considered to be the first destructive motion.

– Destructive Motion 2: Zero effective stress was reached at sensors P2, P3, and P4. Zero effective stress remained after the end of the motion at P3 and P4, but not P2. This implies sustained liquefaction at P3 and P4, unsustained liquefaction at P2, and no liquefaction at the base of the container.

- UCD6

  – Destructive Motion 1: Zero effective stress was reached at sensors P2, P3, and P4. Zero effective stress remained after the end of the motion at P4, excess pore pressure started to dissipate after shaking at P3, and excess pore pressure started to dissipate before the end of the motion at P2. This implies sustained liquefaction only at shallow depths.

  – Destructive Motion 2: Zero effective stress was reached at sensors P3 and P4. Zero effective stress remained after the end of the motion at P4, while excess pore pressure immediately started to dissipate after the motion at P3. Overall, less excess pore pressure was generated during Destructive Motion 1 than Destructive Motion 2 even though the effective PGA was greater in Destructive Motion 2. This implies the model densified during Destructive Motion 1.

  – Destructive Motion 3: Zero effective stress was reached at sensors P2, P3, and P4. Zero effective stress remained after the end of the motion at P3 and P4, but not P2. This implies sustained liquefaction at P3 and P4, unsustained liquefaction at P2, and no liquefaction at the base of the container.

6.3.6   Cone Penetration Test Results

Three cone penetration tests were performed for UCD4, while four were performed for UCD5 and UCD6 (Fig. 6.8). For each model, CPT soundings were performed prior to the first destructive motion and following each destructive motion. An additional CPT sounding was performed at the end of the UCD5 experiment for evaluation of the applicability of the generalized scaling laws to penetration resistance. This will be discussed in more detail in the following paragraphs. All soundings were performed in unique locations within the model.

- UCD4

  – Little change in tip resistance is observed between soundings, indicating the specimen did not densify significantly during shaking. This can be attributed to the model starting dense ($D_R = 84\%$) and relatively low level of shaking.

- UCD5

  – CPT1, CPT2, and CPT3 were performed with a centrifuge scaling factor of $\eta = 21.9$ and a virtual scale factor of $\mu = 2$. CPT4 was performed with a centrifuge scaling factor of $\eta = 43.8$ and a virtual scale factor of $\mu=1$, as tests
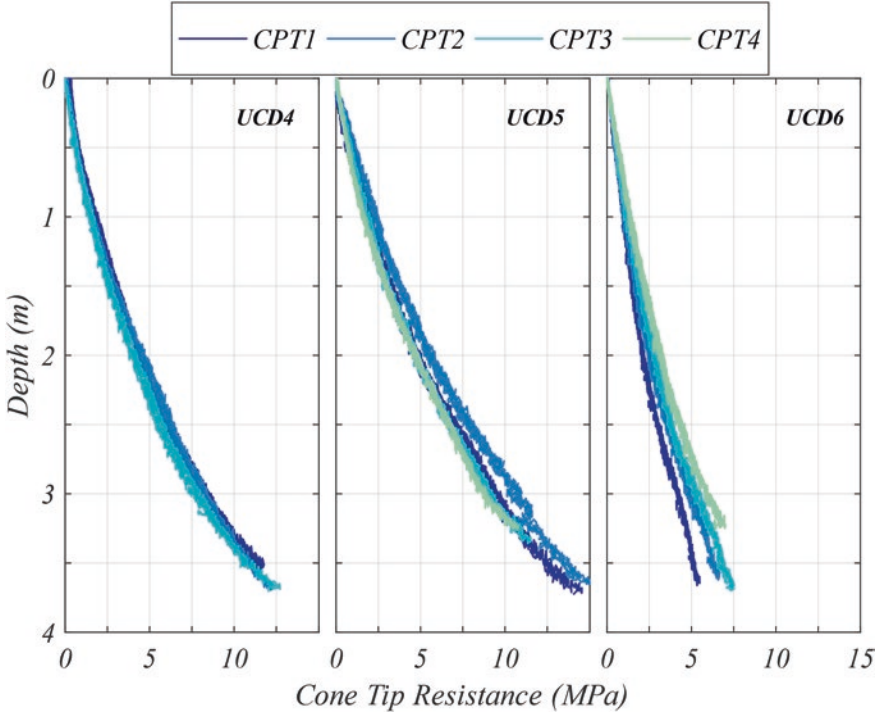
Fig. 6.8 CPT results from UCD4, UCD5, and UCD6

performed using conventional scaling laws. CPT4 was performed to assess the applicability of the generalized scaling laws to cone penetration tests. CPT4 lies on top of CPT3, indicating that generalized scaling laws appear applicable for cone penetration tests for this range of virtual scale factors.

– CPT2 showed greater tip resistance than CPT1, CPT3, or CPT4, which were almost identical. Because all other CPTs were so similar and there were no signs of liquefaction during Destructive Motion 1 in the PPT or accelerometer responses, this increase is likely attributed to spatial variability of density than densification due to shaking. As in UCD4, densification likely did not occur because the model was dense to begin with and shaking intensity was relatively low.

• UCD6.

– At 2 m depth, the cone tip resistance increased by 18% during M1, 13% during M2, and 12% during M3. At 3 m depth, the cone tip resistance increased by 16% during M1, 9% during M2, and 10% during M3. The increased tip resistance is attributed to densification, as this model began at a medium dense state ($D_R = 68\%$).
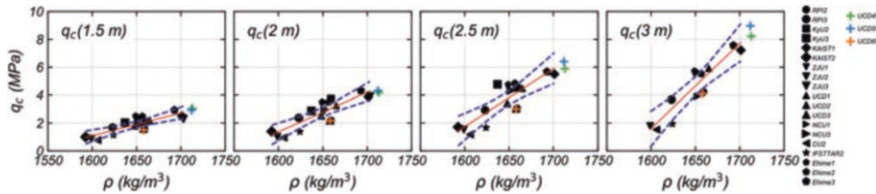
Fig. 6.9 Comparison of CPT results to correlations from LEAP-UCD-2017 (2017 data in black)

– Comparing two models of the same density, UCD6 to UCD3 (from LEAP-UCD-2017, Carey et al., 2020), UCD3 experienced approximately 5% increase in tip resistance at 2 m depth over each destructive motion, significantly less than the 18% and 13% during M1 and M2 of UCD6, respectively.

– Figure 6.9 shows the correlation between cone tip resistances prior to the first destructive motions and measured dry density from the LEAP-UCD-2017 data. The data points from the 2017 tests are shown in black, while the data points from LEAP-ASIA-2018 UCD experiments are shown in color. Overall, the correlation was able to predict the measured dry density of UCD4, UCD5, and UCD6 at various depths. The cone tip resistances used to build the correlation were taken from tests using conventional scaling laws; however, the correlation was able to predict the dry density for UCD5, which was performed using generalized scaling laws. This is a further indication that generalized scaling laws may be applicable to cone penetration tests in this sand.

6.4   Unique Aspects of UCD Experiments

6.4.1   GeoPIV Surface Survey

LEAP-GWU-2015 showed inconsistent displacement patterns attributed to variability in hand measurements of surface markers (Kutter et al., 2018); thus, a better method for displacement measurement is necessary. Prior to now, there has been little success in using conventional sensors to monitor displacement of a submerged curved slope. Displacement transducers have been used, but others (Fiegel & Kutter, 1994) have observed their measurements to be unreliable during liquefaction. During LEAP-UCD-2017, the UCD team designed and developed a new procedure for tracking lateral surface displacements of a centrifuge model using a wave suppressing window, GoPro cameras, and GeoPIV software (Carey et al., 2018a). This procedure was implemented in UCD's experiments for LEAP-UCD-2017. The bottom of the wave suppressing window is below the curved water surface to reduce the reflection of light, like a glass-bottomed boat. A 57 mm gap between the window and the side walls of the container allows for a free water surface to ensure that window confinement does not cause dynamic water pressure oscillation. Five GoPro cameras recording at 240 fps were mounted above the acrylic window (Figs. 6.10
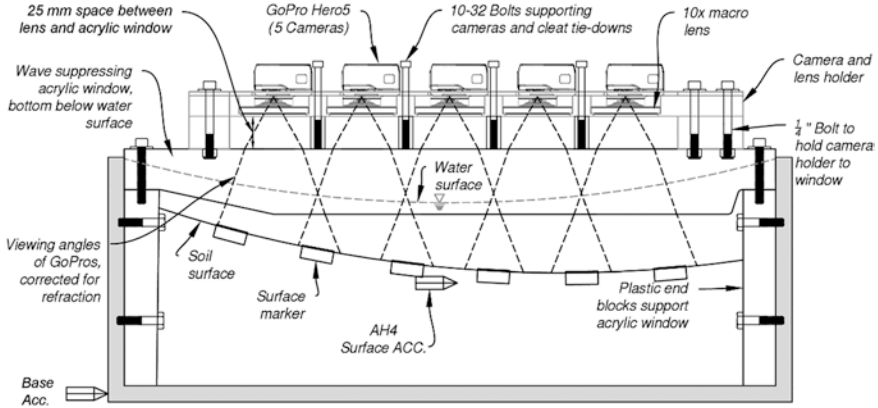
Fig. 6.10 Profile view of centrifuge container with acrylic glass window, GoPro cameras, and macro lenses
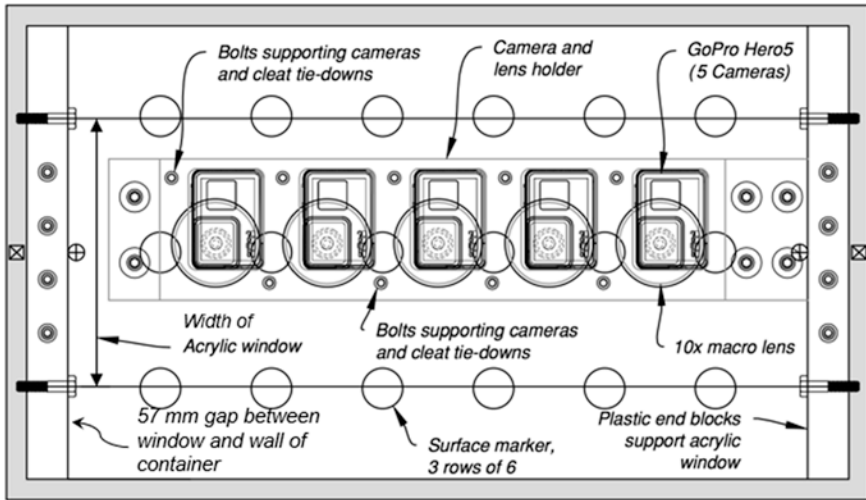

Fig. 6.11 Top view of centrifuge container with acrylic glass window, GoPro cameras, and macro lenses

and 6.11), each viewing through a 10x macro lens, allowing for a sharply focused image of the soil surface. Movement of the first and last surface markers are viewed by one camera each, while movement of the interior four surface markers (2–5) are viewed by two cameras each. Videos recorded from the five GoPro cameras were converted to a series of images using MATLAB and then processed using GeoPIV, an open-source software, which has been used extensively for geotechnical applications and centrifuge testing (Stanier et al., 2015). Displacements were converted
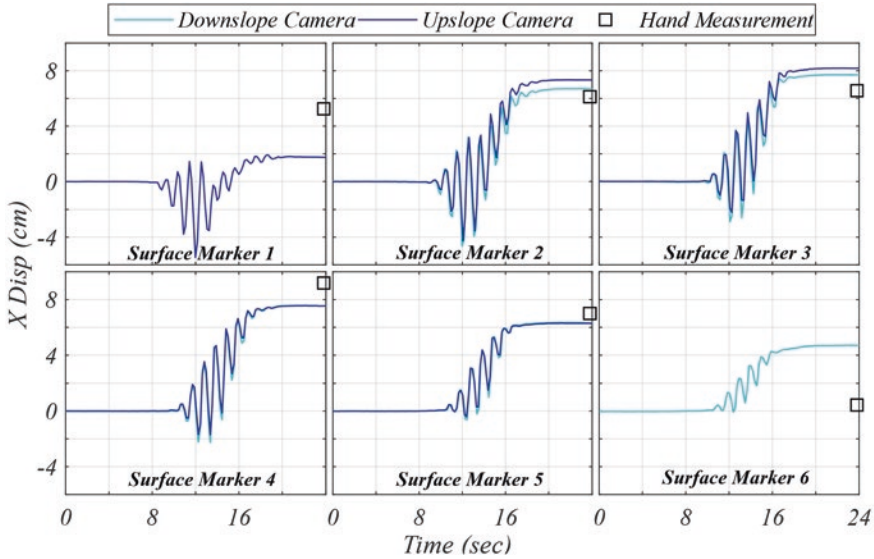
Fig. 6.12 X displacement time history (prototype scale) of six centerline surface markers during UCD6 M1

from pixels to mm using a process described in Carey et al. (2018a), with a camera-specific calibration factor. Figure 6.12 shows the displacement time histories of the six centerline surface markers from UCD6 Destructive Motion 1 found using GeoPIV and compares the final residual displacement to that measured by hand.

Another limitation in measuring surface displacements of centrifuge experiments is spatial density of measurements. The number of surface markers or displacement transducers that can fit into a model is limited, making it difficult to characterize spatial variability of displacements during liquefaction. Using the procedure developed, a grid of patches, or areas to be tracked, across each image is defined during the GeoPIV processing stage. For the UCD experiments, each image was processed using a patch size of 60 pixels square, which corresponds to approximately 10–15 mm square in model space (this varies between cameras). Figures 6.13, 6.14, and 6.15 each show x, y, and z (all dimensions in model scale) displacements from UCD4, UCD5, and UCD6, respectively. Displacements in the x and y directions were found using GeoPIV; some gaps in data are seen due to low image quality in these regions. For the centerband of patches, those within ±40 mm of the container's centerline, z displacements were interpolated using a cubic spline between the centerline surface marker measurements (measured by hand). Although not reported herein, Stone (2019) describes how principles of photogrammetry can be applied to deduce vertical displacements for regions tracked by two cameras.
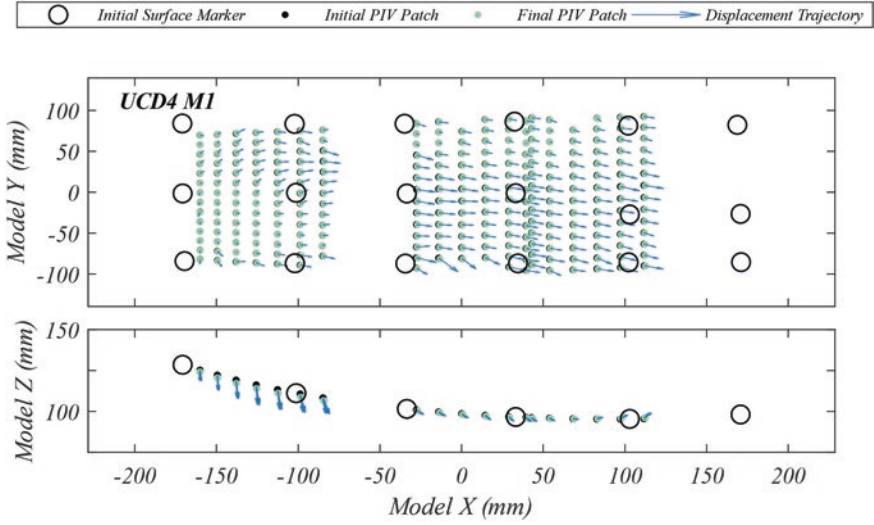
Fig. 6.13 Top and centerline profile views of model scale displacements found using GeoPIV, surface maker measurements, and cubic spline interpolation during UCD4 M1
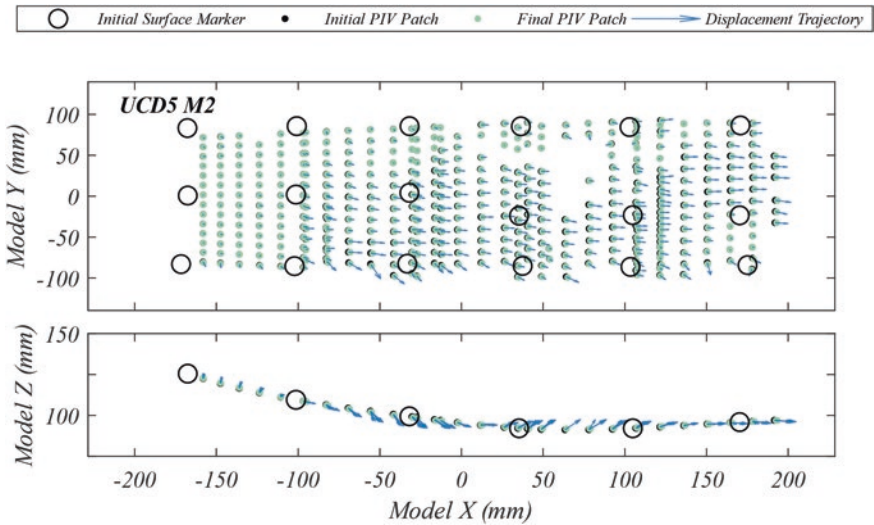

Fig. 6.14 Top view and centerline profile view of model scale displacements found using GeoPIV, surface maker measurements, and cubic spline interpolation during UCD5 M2 (almost no displacement during Destructive Motion 1)
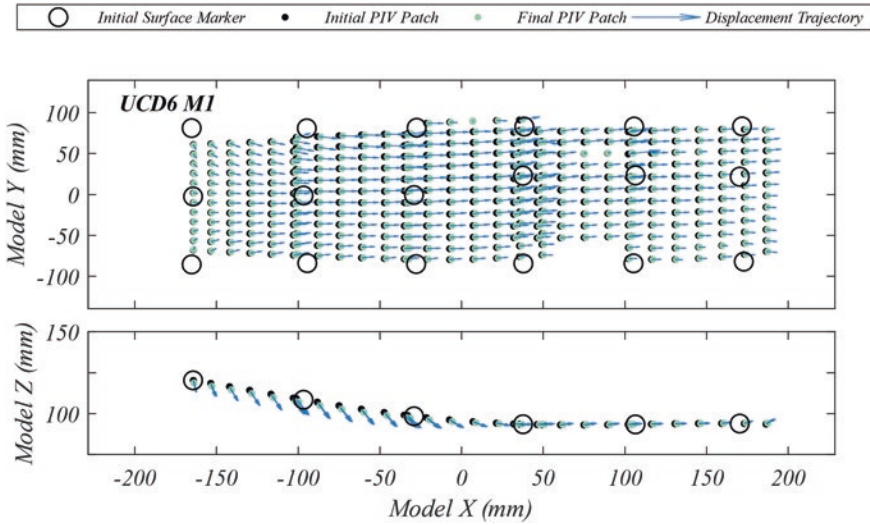
Fig. 6.15 Top view and centerline profile view of model scale displacements found using GeoPIV, surface maker measurements, and cubic spline interpolation during UCD6 M1

6.4.2   Vertical Accelerations due to the Coriolis Effect

As shown in Fig. 6.5, vertical accelerations were observed during each destructive motion. Two sources were hypothesized for their excitation: vertical rocking of the container and the Coriolis effect. Figure 6.16 shows the vertical acceleration time histories, taken as the average from accelerometers AV1 and AV2, located on opposite ends of the container. When comparing the time histories in Fig. 6.16 to those seen in Fig. 6.5, there is no longer the presence of a 3 Hz component, indicating that the 3 Hz component was due to rocking. This is corroborated in Fig. 6.5 by observing that the 3 Hz components of AV1 and AV2 are approximately 180 degrees out of phase.

The theoretical Coriolis acceleration for each destructive motion was calculated using the following vector cross product:

$$a_{\text{Coriolis}} = 2\Omega \times V_{\text{rel}} \tag{6.1}$$

where V_{rel} is found by time integration of the input base acceleration (average of AH11 and AH12) and Ω is the angular velocity of the spinning centrifuge. Figure 6.16 compares the theoretical Coriolis accelerations to the average recorded vertical accelerations. Superimposed on these time histories are the absolute cumulative normalized errors between theoretical and observed vertical accelerations. As well, the time at end of shaking is noted. During all destructive motions of UCD4 and UCD6, the vertical accelerations were under-predicted, and free vibration after the end of
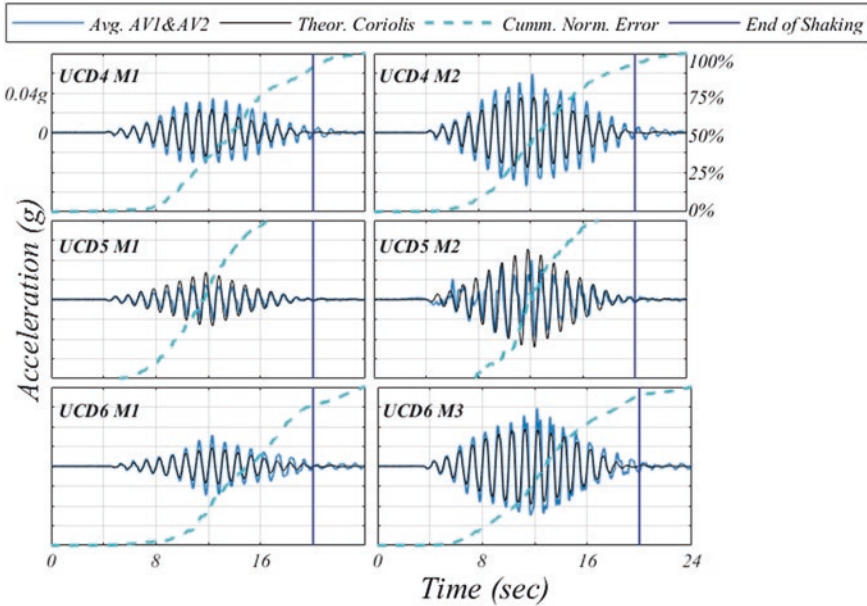
Fig. 6.16 Theoretical Coriolis acceleration versus average vertical acceleration for UCD4, UCD5, and UCD6

shaking is observed. During UCD5, the vertical accelerations were over-predicted, and no free vibration after the end of shaking is observed. This indicates that vertical vibration resonance of the shaker system was activated during UCD4 and UCD6, but not during UCD5. Using the generalized scaling laws, different shaking frequencies were used in UCD5 than in the other tests; however, all motions were intended to represent 1 Hz in prototype scale. UCD4 and UCD6 were performed with a 1 g scale factor of $\mu = 1$ and centrifuge scale factor of $\eta = 43.8$, thus requiring 43.8 Hz model scale input motion. UCD5 was performed with a 1 g scale factor of $\mu = 2$ and centrifuge scale factor of $\eta = 21.9$, thus requiring 36.8 Hz model scale input motion (see Table 6.1 for time scale factor equation). A consequence of resonance is that vertical vibrations continuing after the end of shaker excitation (time = 20 s) could result in slower pore pressure dissipation and larger displacements.

6.4.3 Reversed Slope in UCD6

The presence of vertical acceleration due to Coriolis effect may have other implications on model performance beyond the effect of additional vertical shaking cycles due to resonance. Since the Coriolis acceleration is a function of V_{rel} (found by integration of the horizontal base acceleration), it is 90 degrees out of phase with the

horizontal base acceleration, resulting in an elliptical displacement trajectory of the container during shaking. Figure 6.17(a) shows the container's horizontal and vertical displacement time histories during UCD6 M1. Horizontal displacement was found by double time integration of the filtered base acceleration (average of AH11 and AH12 processed through a 0.3–3 Hz fourth-order bandpass filter). The vertical displacement was found by double integration of the filtered vertical acceleration (average of AV1 and AV2 processed through a 0.3–3 Hz fourth-order bandpass filter). As expected, the vertical displacement is out of phase with the horizontal displacement by 90 degrees, reinforcing the conclusion that the vertical accelerations are due to the Coriolis effect. This results in a counterclockwise elliptical displacement trajectory (Fig. 6.17(b)); this is true for every UCD destructive motion.

It was hypothesized that the direction of the container trajectory, with respect to the model slope, could affect model performance. To test this hypothesis, UCD6 was built with a reversed slope, but at the same initial density (1658 kg/m^3) as UCD3. Figure 6.18 shows slope orientations of UCD3 (left) and UCD6 (right) with respect to the counterclockwise elliptical displacement trajectory of the container. The hypothesis is that the counterclockwise trajectory could inhibit downslope
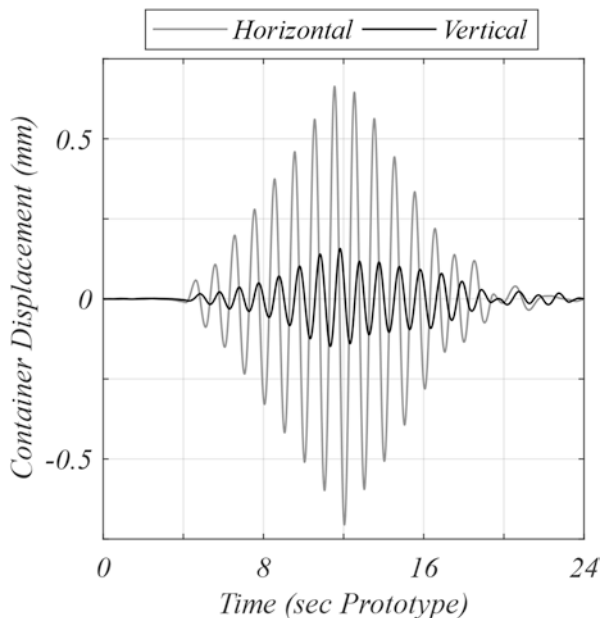

Fig. 6.17 (**a**) Horizontal and vertical displacement time histories of model container during UCD6 M1. (**b**) Vertical/horizontal container displacement during UCD6 M1
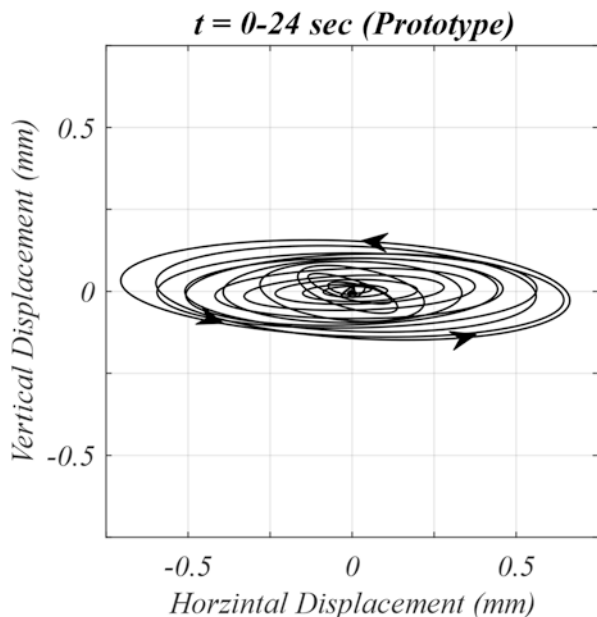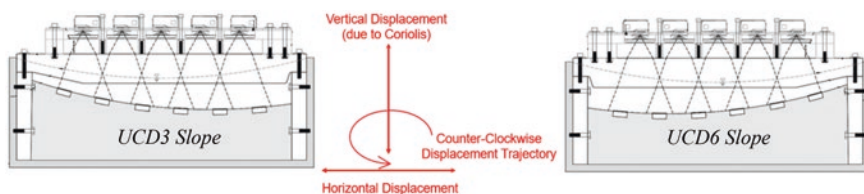
Fig. 6.17 (continued)

Fig. 6.18 Opposite slope geometry of two UCD models with respect to counterclockwise elliptical displacement trajectory

displacement for the UCD3 slope orientation and could exacerbate downslope displacement for the UCD6 slope orientation. Figure 6.19 compares hand-measured lateral and vertical surface marker displacements from UCD3 M1 and UCD6 M1.

A larger base acceleration was input during UCD3 M1 ($PGA_{eff} = 0.174$ g) than UCD6 M1 ($PGA_{eff} = 0.137$ g). This is reflected by the fact that UCD3 M1 experienced larger lateral displacements than UCD6 M1. However, Fig. 6.19 also shows that vertical displacements were slightly greater in UCD6 than UCD3, the primary component of displacement in UCD6 being vertical.

Figure 6.20 shows CPT soundings before and after M1 from both UCD3 and UCD6. It is shown that CPT1 from UCD3 and UCD6 are almost identical, as the models began with the same initial density; however, UCD6 experienced greater increase in tip resistance than UCD3, on average over the depth of the push. This may be attributed to densification during strong shaking. Although it is not
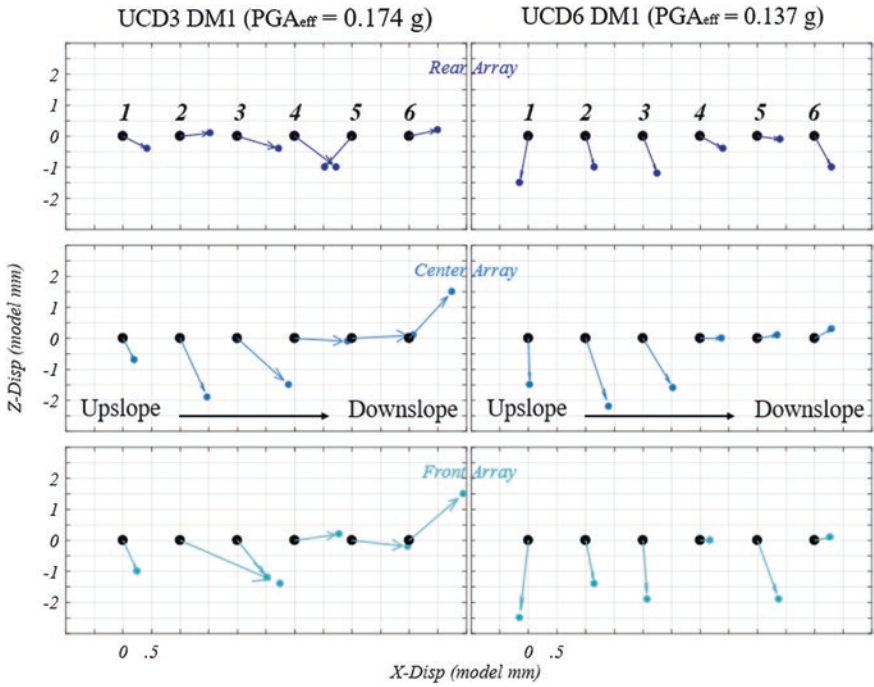
Fig. 6.19 Profile view comparison of hand-measured lateral and vertical surface marker displacements from UCD3 M1 (left) and UCD6 M1 (right). Each test is shown upslope to downslope as left to right for ease of comparison
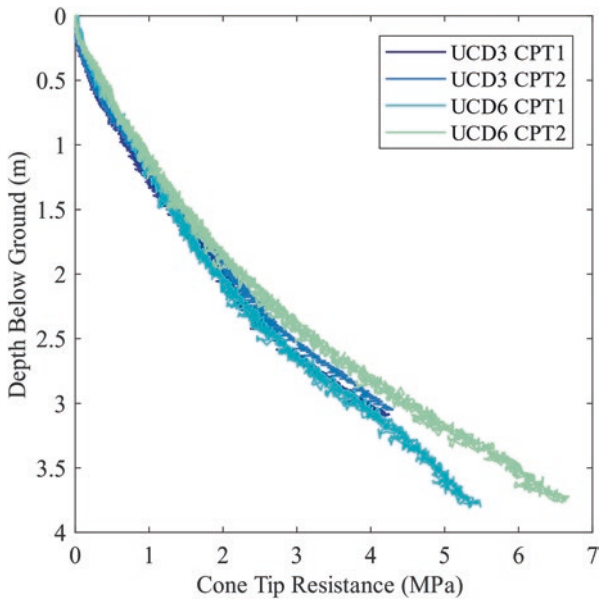

Fig. 6.20 Comparison of CPT profiles before and after M1 for UCD3 and UCD6

conclusive, as this is only one test comparison, it may be that reversing the slope in UCD6 may affect model performance, causing increased vertical settlement and densification for a smaller ground motion.

It should be noted that vertical accelerations due to the Coriolis effect will only arise if shaking occurs in the circumferential direction, and the influence of the Coriolis effect increases as the radius of the centrifuge arm decreases. Because the Coriolis acceleration is proportional to the angular velocity (Eq. 6.1), it is inversely proportional to the square root of the centrifuge radius (Eq. 6.2).

$$a_{\text{Coriolis}} = 2 * \sqrt{\frac{\mu * \eta}{r_{\text{centrifuge}}}} \times V_{\text{rel}} \qquad (6.2)$$

6.5 Method for Measuring Dry Density

The procedure to measure specimen density for the LEAP-ASIA-2018 UCD experiments follows the procedure described by Carey et al. (2020). Density was calculated by mass and volume measurements at several points during model construction to check the target density was being reached consistently throughout the model depth. At each intermediate check, the surface was vacuumed flat, 15 locations were measured and then averaged, and the density was calculated using the mass of the lift.

Reported density of the model used volume and mass measurement of the final curved surface. The model height was measured at 11 locations along 3 longitudinal lines of the final curved surface, for a total of 33 measurements. Using AutoCAD, a curve was fit to the 11 points on the same longitudinal line. The area of each region was calculated, and then the model volume was taken as the average of the three cross-section areas multiplied by the 279 mm width of the container. Density was then calculated using the final mass of the model. The LEAP-ASIA-2018 test template contains supplemental documentation of density calculation for each lift during construction, including the final curved surface.

6.6 Viscous Fluid Preparation and Saturation

6.6.1 Viscous Fluid Preparation

Methylcellulose was used for each UCD experiment to scale pore fluid viscosity in accordance with the generalized scaling law, visc = visc$_{\text{water}}$ $*$ $\mu^{0.75}$ $*$ η. Prior to centrifuge testing, several batches of viscous solution were mixed to determine the correct proportion of Dow, F50 Food Grade hydroxypropyl methylcellulose power

and water, by mass, to achieve the desired viscosity. The ratio of mass of methylcel-lulose to mass of water for Type A ($\mu = 1$, $\eta = 43.75$) and Type B ($\mu = 2$, $\eta = 21.89$) tests were approximately 2.2% and 1.8%, respectively.

The methylcellulose was prepared in accordance with the chemical supplier rec-ommendation for hot mixed solution. The procedure was as follows:

1. Warm roughly 1/4 of the required deionized water to 90 °C. Add methylcellulose with a mass that is equal to 8.8% of mass of the deionized water.
2. Mix solution for 45 min.
3. Dilute the mixture with the same mass of water from step 1 at room temperature. Mix for additional 10 min. Following mixing, the solution should be at roughly double concentration.
4. Cool overnight.
5. Using an approximately 200 g sample of the stock solution, 208 g of room tem-perature deionized water was added and mixed. Viscosity of the solution was checked using a Cannon instrument size 2 Ubbelohde viscometer.
6. Step 5 was repeated if necessary, adjusting the amount of deionized water added, to determine the correct ratio of deionized water and stock until the desired vis-cosity is obtained.
7. Lastly, the entire batch of methylcellulose was mixed with the correct ratio of water and stock found in step 6.

6.6.2   Saturation

The same saturation procedure, as presented in Carey et al. (2020), was followed for each of the UCD models. Initially, the dry model and container were placed in a vacuum chamber. 97 kPa of vacuum was applied, and then the vacuum was shut off, and the chamber was flooded with CO_2, until the vacuum was reduced to 1–2 kPa. The CO_2 flow was then shut off, and 97 kPa vacuum was reapplied. This cycle was repeated two more times. Following the third evacuation, the residual concentration of nitrogen and oxygen gas in the chamber should be $\left(\dfrac{101.4 - 97}{101.4}\right)^3 = 0.008\%$ of its initial concentration. The methylcellulose solution was de-aired and dripped onto a sponge located on the top surface of the sand. A pool of de-aired methylcellulose solution was maintained in the lowest edge of the container. As the wetting front progressed toward the top of the model, the size of the pool was allowed to grow. The top corner of the slope was the last portion of the model to saturate in order to avoid entrapping residual gas within the model. 97 kPa vacuum was maintained throughout the infiltration of methylcellulose. Once the model was completely satu-rated and the surface submerged, the vacuum was slowly released.

The degree of saturation was then checked using the method described in the specification (Kutter et al. 2019), modified from Okamura and Inoue (2012). The vacuum chamber was opened, and a tethered float, delineated with a 1 cm grid, was
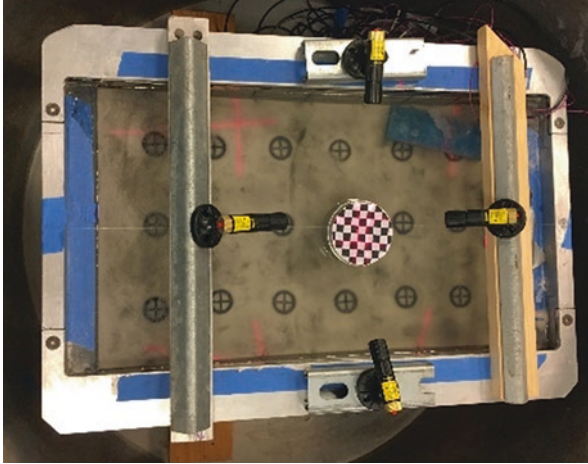
Fig. 6.21 Lasers positioned so lines make cross-hair at float on surface of methylcellulose

placed on the methylcellulose surface. Laser pointers were positioned on the container walls pointing downward at the floating grid with a 5-degree angle. The laser pointer and float configuration are shown in Fig. 6.21. The transparent cover was placed back over the vacuum chamber, and the locations of the lines from the lasers on the float were noted. A 10 kPa vacuum was applied, and the locations of the laser lines were recorded again. Changes in the location of the laser lines are presumed to be caused by volume change of trapped gas in the model. Using Boyle's law, the volume of air and degree of saturation can be estimated. No movement of the laser lines was observed for each of the experiments, so the degree of saturation was estimated to be better than 99.99%. The corresponding CO_2 gas content is 0.01% of the viscous fluid volume, which could easily dissolve in the viscous fluid during spinning.

6.7   Conclusions

This paper describes the three experiments performed on the 1 m centrifuge at the University of California, Davis as part of the LEAP-ASIA-2018 exercise. Two experiments were performed using conventional centrifuge scaling laws, and one experiment was performed using generalized scaling laws. The model performance and results for multiple destructive ground motions were presented. Two unique aspects of the tests performed were also discussed: using GeoPIV to measure surface displacements and the implications of the Coriolis effect on model performance. Additionally, methods for measuring dry density, mixing viscous fluid, and model saturation are explained.

Destructive Motion 1 in UCD5 did not cause liquefaction, which is evident by the low excess pore pressures and nearly rigid acceleration response. For this

reason, Destructive Motion 2 in UCD5 may be better suited for comparisons. Liquefaction was observed for all other motions. A third, very large, destructive motion was performed in UCD6 to cover a broad range of ground motion intensities. Little to no change in cone tip resistance was observed in UCD4 or UCD5, due to their high initial densities and relatively low level of shaking; however, cone tip resistance increased during each destructive motion in UCD6, due to its initially medium dense state. A fourth CPT was performed at the end of UCD5, to compare soundings under conventional and generalized scaling; the results coincided nicely.

GeoPIV was used to survey surface displacements during each experiment. Its use allowed for time histories of displacement and greater spatial resolution of measurements. Displacement patterns were consistent with other sensors in their indication of liquefaction severity. Final displacements, as measured by GeoPIV, also matched surface marker hand measurements reasonably well.

The cause of non-specified vertical accelerations during each destructive motion was attributed to the Coriolis effect. Additional cycles of vertical shaking were measured in UCD4 and UCD6, attributed to resonance in the shaker system being activated by the input acceleration frequency. Time integrating container mounted horizontal and vertical accelerometers showed the container displacement trajectories followed a counterclockwise elliptical trajectory for every motion. Comparing surface marker and CPT data from two models of the same initial density (UCD3 and UCD6) showed that slope orientation with respect to this orientation may affect model performance.

References

Carey, T. J., Hashimoto, T., Cimin, D., & Kutter, B. L. (2017). LEAP-GWU-2015 centrifuge test at UC Davis. *Soil Dynamics and Earthquake Engineering*. https://doi.org/10.1016/j. soildyn.2017.01.030

Carey T. J., Stone, N., Kutter, B. L, & Hajialilue-Bonab, M. (2018a). A new procedure for tracking displacements of submerged sloping ground in centrifuge testing. In *Proceedings of the 9th International Conference on Physical Modelling in Geotechnics 2018 (ICPMG 2018)* London, United Kingdom.

Carey T. J., Kutter, B. L., Haigh, S. K., Madabhushi, S. P. G., Okamura, M., Kim, D. S., Ueda, K., Hung, W. Y., Zhou, Y. G., Liu, K., Chen, Y. M., Zeghal, M., Abdoun T., Esco_er, S., & Manzari, M. (2018b). A new shared miniature cone penetrometer for centrifuge testing. In *Proceedings of the 9th International Conference on Physical Modelling in Geotechnics 2018 (ICPMG 2018)* London, United Kingdom.

Carey T. J., Stone N., Bonab M. H., & Kutter B. L. (2020). LEAP-UCD-2017 centrifuge test at University of California, Davis. (In press).

Fiegel, G. L., & Kutter, B. L. (1994). Liquefaction Mechanism for Layered Soils. *Journal of Geotechnical Engineering, 120*, 737–755. https://doi.org/10.1061/ (asce)0733-9410(1994)120:4(737)

Iai, S., Tobita, T., & Nakahara, T. (2005). Generalized scaling relations for dynamic centrifuge tests. *Geotechnique, 55*(5), 355–362.

Kutter, B., Carey, T., Hashimoto, T., Zeghal, M., Abdoun, T., Kokalli, P., Madabhushi, G., Haigh, S., Hung, W.-Y., Lee, C.-J., Iai, S., Tobita, T., Zhou, Y. G., Chen, Y., & Manzari, M. T. (2018). LEAP-GWU-2015 experiment specifications, results, and comparisons. *Soil Dynamics and Earthquake Engineering, 113*, 616–628. https://doi.org/10.1016/j.soildyn.2017.05.018

Kutter, B. L., Carey, T. J., Stone, N., Bonab, M. H., Manzari, M. T., Zeghal, M., Escoffier, S., Haigh, S. K., Madabhushi, G. S. P., Hung, W.-Y., Kim, D.-S., Kim, N. R., Okamura, M., Tobita, T., Ueda, K., & Zhou, Y.-G. (2019). LEAP-UCD-2017 V. 1.01 Model Specifications. In Model Tests and Numerical Simulations of Liquefaction and Lateral Spreading (pp. 3–29). Springer International Publishing. https://doi.org/10.1007/978-3-030-22818-7_1

Okamura, M., & Inoue, T. (2012). Preparation of fully saturated models for liquefaction study. *International Journal of Physical Modelling in Geotechnics, 12*, 39–46. https://doi.org/10.1680/ijpmg.2012.12.1.39

Stanier, S. A., Blaber, J., Take, W. A., & White, D. J. (2015). Improved image-based deformation measurement for geotechnical applications. *Canadian Geotechnical Journal, 53*(5), 727–739.

Stone N. S. (2019). MSc thesis, Department of Civil and Environmental Engineering, University of California, Davis (In preparation).